



Magnetic ordering tendencies in hexagonal-boron-nitride–bilayer-graphene moiré structuresMaria Spethmann ¹, Carsten Honerkamp,¹ and Dante M. Kennes ^{2,3}¹*Institute for Theoretical Solid State Physics, RWTH Aachen University,
and JARA Fundamentals of Future Information Technology, 52056 Aachen, Germany*²*Institute for Theory of Statistical Physics, RWTH Aachen University,
and JARA Fundamentals of Future Information Technology, 52056 Aachen, Germany*³*Max Planck Institute for the Structure and Dynamics of Matter,
Center for Free Electron Laser Science, Luruper Chaussee 149, 22761 Hamburg, Germany*

(Received 30 May 2021; accepted 13 August 2021; published 25 August 2021)

When hexagonal boron nitride (hBN) and graphene are aligned at zero or a small twist angle, a moiré structure is formed due to the small lattice constant mismatch between the two structures. In this paper, we analyze magnetic ordering tendencies, driven by on-site Coulomb interactions, of encapsulated bilayer graphene (BG) forming a moiré structure with one (hBN-BG) or both hBN layers (hBN-BG-hBN), using the random phase approximation. The calculations are performed in a fully atomistic Hubbard model that takes into account all π electrons of the carbon atoms in one moiré unit cell. We analyze the charge neutral case and find that the dominant magnetic ordering instability is uniformly antiferromagnetic. Furthermore, at low temperatures, the critical Hubbard interaction U_c required to induce magnetic order is slightly larger in those systems where the moiré structure has caused a band gap opening in the noninteracting picture, although the difference is less than 6%. Mean-field calculations are employed to estimate how such an interaction-induced magnetic order may change the observable single-particle gap sizes.

DOI: [10.1103/PhysRevB.104.085147](https://doi.org/10.1103/PhysRevB.104.085147)**I. INTRODUCTION**

Hexagonal boron nitride (hBN) is frequently used as a substrate for graphene devices, because it offers a flat and clean surface and enables a high charge carrier mobility [1]. When single-layer graphene (SG) and hBN are stacked at no or a small twist angle to each other, they form a moiré structure due to a small lattice constant mismatch. hBN has a lattice constant of around $a_{\text{hBN}} = 0.2504$ nm [2] whereas SG has a lattice constant of $a = 0.246$ nm [3]. The formed moiré structure, with lattice constants up to 14 nm [4], changes the electronic properties of the material and has been analyzed in several theoretical [5–8] and experimental [9–11] papers. For example, a band gap opens at the central Dirac points of SG [11]. The size of the central band gap was analyzed in calculations, which stressed the importance of the structural relaxation of the carbon atoms within the moiré structure, but also included many-body perturbation theory and electron-electron interactions [6,12]. Further, secondary, gapped Dirac points have been reported to form at the mini Brillouin zone edges [1,8]. In addition, the wavelength of the moiré structure and the underlying potential modulation is well suited to observe the Hofstadter butterfly, a self-similar pattern of the energy levels as a function of a magnetic field [10,11].

In contrast to hBN-SG systems, literature on hBN–bilayer graphene (BG) and hBN-BG-hBN moiré structures is less extensive. In Ref. [8], the band structure of hBN-BG was calculated in a tight binding model that explicitly took the boron and nitrogen atoms into account. Then an effective

continuum model was used to calculate the spectrum featuring Hofstadter’s butterfly. In Ref. [13], n -layer structures built of graphene and hBN were analyzed theoretically, including interaction effects and a vertically applied electrical field, which contributes to the formation of flat bands and changes the Chern number. Further, correlated states such as quantum anomalous Hall insulating states and fractional anomalous quantum Hall effect states were described. In the experimental work of Ref. [14], band gap widths were measured at the central Dirac point and the secondary Dirac points both in hBN-SG and hBN-BG samples. It was found that in hBN-BG the secondary Dirac points are not fully gapped, and the particle-hole asymmetry is less pronounced compared to hBN-SG. The measurements were accompanied by theoretical calculations and it was concluded that the observed behavior can be explained qualitatively in a noninteracting picture. Another experimental study created doubly aligned hBN-BG-hBN with a close-to-zero rotation angle [15]. They measured a nonlocal resistance which they attribute to a “valley current” near the band gap at charge neutrality. In Ref. [16], doubly aligned hBN-BG-hBN was produced with a small twist in one hBN layer and resistivity measurements displayed secondary Dirac points from both moiré structures.

In this paper, we want to understand hBN-BG and hBN-BG-hBN moiré structures more comprehensively by analyzing interaction-driven magnetic order [17]. This magnetic order is relevant as a proxy for interaction-induced gaps in BG and is a promising candidate for the cases where such interaction-induced gaps may have been observed. In

fact, in a number of experiments on freely suspended few layers [18,19–21] and multilayers [22–24] of graphene, all in Bernal stacking, evidence for an interaction-induced gap opening was found. This was interpreted theoretically as due to layered-antiferromagnetic order [25–31]. In theory, also SG hosts this ordering tendency [32], but the density of states at low energies is not as high as in the layered systems, and hence the ordering instability does not occur under normal circumstances. Clearly, it is of interest how this ordering tendency of layered graphene is altered in the presence of an hBN environment. The influence of the aligned hBN is twofold: First, it modifies the band structure, which is addressed in this paper. Second, the hBN environment leads to additional screening of the electron-electron interactions. This effect is, e.g., dealt with by Roesner *et al.* [33] and can be incorporated in our reasoning by choosing an appropriately renormalized interaction constant.

Our calculations for the interaction effects are restricted to charge neutrality and zero external magnetic field. First, we extend the hBN-SG model of Ref. [34] to a model of hBN-BG and hBN-BG-hBN. In this process we also distinguish between different stacking configurations. Next, we calculate the parameters for which the interacting spin susceptibility diverges in the random phase approximation (RPA). This provides information about the dominant magnetic order of these systems. Finally, we compare our RPA results to mean-field calculations, where we are able to calculate the band gap widths of the magnetic phases.

II. METHODS

We set up a Hubbard model that describes the π electrons of the carbon atoms, where each atom provides one orbital:

$$H = \sum_{\substack{\mathbf{R}_1, \mathbf{R}_2, \\ r_1, r_2, \sigma}} -t(\mathbf{d})c_{\mathbf{R}_1, r_1 \sigma}^\dagger c_{\mathbf{R}_2, r_2 \sigma} + U \sum_{\mathbf{R}, \sigma} n_{\mathbf{R}, \sigma \uparrow} n_{\mathbf{R}, \sigma \downarrow} + \sum_{\mathbf{r}, \mathbf{R}, \sigma} \epsilon_{\mathbf{r}}^{\text{hBN}} c_{\mathbf{R}, r \sigma}^\dagger c_{\mathbf{R}, r \sigma}. \quad (1)$$

The field operators $c_{\mathbf{R}, r \sigma}^{(\dagger)}$ annihilate (create) an electron with spin σ at a site with lattice vector \mathbf{R} and basis vector \mathbf{r} . The atomic positions and the tight binding part including the hopping parameter $t(\mathbf{d})$, which is a function of the distance \mathbf{d} , are constructed as explained in Refs. [35,36], a model originally used to describe twisted bilayer graphene. We fix the interlayer distance to be $d_{AB} = 0.335$ nm [3]. The interaction is a Hubbard on-site interaction of strength U and the operators $n_{\mathbf{R}, r \sigma}$ are the spin-dependent electron density operators. Although screening effects are less pronounced in graphene materials, and therefore the nearest-neighbor interaction is comparable to an on-site interaction [37], a description using the on-site interaction only is justified when U is properly renormalized [38,39].

The boron and nitrogen electrons are not taken into account explicitly in our model. Instead, the moiré structure is modeled by an effective potential term $\epsilon_{\mathbf{r}}^{\text{hBN}}$ on the carbon atoms, as proposed for hBN-SG in Ref. [34]. There, a commensurate moiré structure is assumed with adjusted lattice constants to form a well-defined moiré unit cell. A close approximation

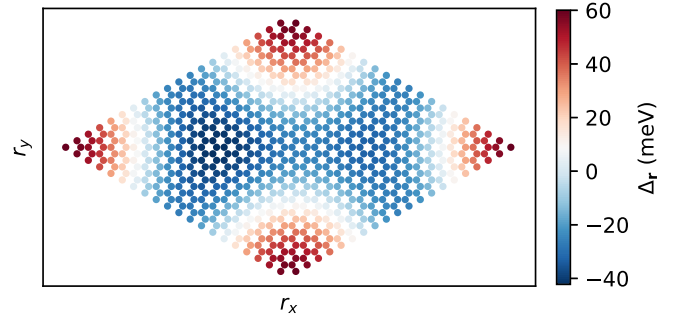


FIG. 1. The “hBN potential” Δ_r acting on the carbon sites at position $\mathbf{r} = (r_x, r_y)$, as adapted from Ref. [34]. The carbon sites are shown within one moiré unit cell of artificially decreased size ($N_{\text{moiré}} = 20$).

would be $\frac{a}{a_{\text{hBN}}} \approx \frac{55}{56}$ [2,8]. But since this requires a very large unit cell (with a lattice constant a factor $N_{\text{moiré}} = 56$ larger than in graphene) and extensive computational resources, we perform our calculations on a simplified model with $\frac{a}{a_{\text{hBN}}} \approx \frac{19}{20}$ ($N_{\text{moiré}} = 20$), unless marked otherwise. This means each unit cell in the moiré structure contains $N_{\text{moiré}} \times N_{\text{moiré}} \times 4$ carbon atoms. In Ref. [34] an effective potential on the carbon atoms from the hBN layer was proposed by performing a fit to density functional theory (DFT) results. We repeated the last part of the fit using the same fit data points but a different function that keeps the threefold rotational symmetry:

$$\Delta_r = A(\sin(\mathbf{G}_1 \cdot \mathbf{r} + \phi) + \sin(\mathbf{G}_2 \cdot \mathbf{r} + \phi) + \sin[-(\mathbf{G}_1 + \mathbf{G}_2) \cdot \mathbf{r} + \phi]) + C. \quad (2)$$

Here, $\mathbf{G}_1, \mathbf{G}_2$ are the reciprocal primitive lattice vectors, and A, ϕ , and C are fit parameters, with best fit results at $A = A_{\text{Fit}} = 21.9$ meV, $\phi = \phi_{\text{fit}} = 1.655$, and $C = C_{\text{Fit}} = -4.7$ meV. In the following, Δ_r will be called the hBN potential and is shown in Fig. 1. The effective potential incorporates Δ_r with alternating sites on the two carbon atoms of the honeycomb lattice,

$$\epsilon_{\mathbf{r}}^{\text{hBN}} = s_{\mathbf{r}} \Delta_r, \quad (3)$$

with $s_{\mathbf{r}} = +1/-1$ for \mathbf{r} being at an A/B site. To set up a model of hBN-BG from this model of hBN-SG, we assume that the substrate only affects the first graphene layer [14], thus the hBN potential is only added on one graphene layer. hBN-BG has two different stacking configurations, as pointed out in Refs. [8,14]. These two structures are shown in Fig. 2, which depicts one region of the moiré structure. For hBN-BG-hBN moiré structures we need to differentiate between more stacking configurations and we concentrate on those configurations where we can determine a clear stacking axis, as shown in Fig. 3. The hBN potential is modified on the second graphene layer as to match a given configuration. For example, in hBN-BG-hBN case 3 the potential on the upper layer is multiplied by minus one and shifted by two-thirds of the moiré cell diagonal. After having properly defined the noninteracting model, we can now take into account the Hubbard interaction and identify the possibility of magnetic order in the material. We calculate the magnetic susceptibility χ^m in RPA by summing up infinitely many diagrams via the

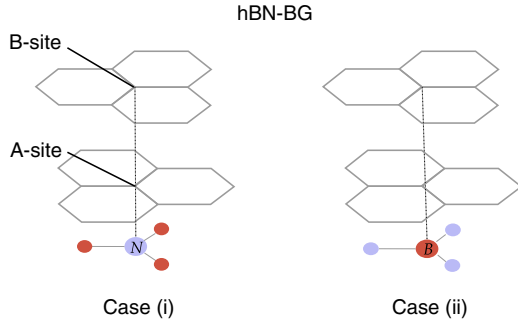


FIG. 2. Different stacking configurations of hBN-BG. The second layer can be positioned such that at the corners of the moiré unit cell (see Fig. 1) the stacking axis either goes through a nitrogen atom [case (i)] or a boron atom [case (ii)].

exchange channel, analogous to Ref. [40], resulting in

$$\hat{\chi}^m = \hat{\chi}(\mathbb{1} + U\hat{\chi})^{-1}. \quad (4)$$

Here, $\hat{\chi}$ is the polarization function

$$\chi_{r,r'}(\omega, \mathbf{q}) = \frac{1}{\beta\Omega} \sum_{\omega'} \int d\mathbf{k} g_{r,r'}(\omega', \mathbf{k}) g_{r',r}(\omega + \omega', \mathbf{k} + \mathbf{q}), \quad (5)$$

a matrix of the size of the number of atoms in the moiré cell. The functions g are the bare Green's functions, $\beta = \frac{1}{T}$ is the inverse temperature ($k_B = 1$), ω, ω' are bosonic and fermionic Matsubara frequencies, the integral is taken over wave vectors \mathbf{k} in the Brillouin zone with area Ω , and \mathbf{q} is the wave vector of the corresponding magnetic spin density wave. The magnetic susceptibility diverges when the ‘‘Stoner denominator,’’ i.e., the matrix $(\mathbb{1} + U\hat{\chi})$ to be inverted, develops a vanishing eigenvalue. This is the case for certain critical values of T and U . Since the interaction strength is a model parameter that is not known exactly, we can calculate the critical interaction strength U_c for fixed temperature via the relation $U_c = -\frac{1}{x_0}$. Here, x_0 is the most negative eigenvalue of the polarization function. U_c marks the minimum interaction strength needed for the system to be in a magnetic phase at fixed temperature. The eigenvector \mathbf{x}_0 corresponding to the eigenvalue x_0 is proportional to the magnetization on each atom, whose magnitude cannot be obtained from this analysis. This is because all other eigenvectors become irrelevant when the spin susceptibility diverges. As in Ref. [40] we evaluate

the Matsubara sum in χ numerically and set $\omega = 0$ for the static case and $\mathbf{q} = \mathbf{0}$ for identical moiré cells.

We also calculate the magnetic order in mean-field theory to compare our results with the RPA calculation. For this, we replace the spin density operator $S_{R,r}^z = \frac{1}{2}(n_{R,r\uparrow} - n_{R,r\downarrow})$ by its mean field $S_{R,r}^z \rightarrow \langle S_r^z \rangle + \delta S_{R,r}^z$ and neglect higher orders of fluctuations $O[(\delta S_{R,r}^z)^2]$ [41]. Further, we neglect terms in the Hamiltonian describing charge density waves, because we want to focus on spin density fluctuations [32]. The resulting noninteracting Hamiltonian (up to a constant)

$$H = \sum_{\substack{r_1, r_2, \\ \sigma, k}} [H_{r_1, r_2}(\mathbf{k}) - \sigma U \langle S_r^z \rangle \delta_{r_1, r_2}] c_{k, r_1 \sigma}^\dagger c_{k, r_2 \sigma} \quad (6)$$

is then solved self-consistently. This allows us to obtain mean-field estimates for interaction-induced energy gaps. These can then be compared with spectral gaps that derive from the ‘‘single-particle’’ description, here primarily from the substrate and stacking.

III. RESULTS

Before we analyze the magnetic order, it is insightful to first understand the impact of the hBN potential defined in Eq. (2) on the noninteracting system. In Fig. 4 we compare the band structure of hBN-BG, with the bands of (free-standing) BG downfolded into the mini Brillouin zone of the composite structure. In agreement with Ref. [14], secondary Dirac points form at the new mini Brillouin zone edges and are split up in hBN-BG. We observe only a small particle-hole asymmetry. In addition, a band gap opens around zero energy. The low-energy band structure mostly determines our results of the magnetic order and is therefore shown as a zoom-in in Fig. 5. In this figure we see two of the four Dirac points around K in free-standing BG that are a result of trigonal warping [37]. In both configurations of hBN-BG a band gap opens. For the studied hBN-BG-hBN configurations the band structures split into two subgroups. In cases 1–3 the band gap opens further compared to the one-sided cases whereas in cases 4–7 the band gap closes again. The good agreement within the subgroups is a result of the fact that the C parameter of the hBN potential is mostly responsible for the band gap opening, while the A parameter does not have a significant influence. In fact, when we set the A parameter to zero we still obtain the same low-energy band structure (Fig. 5). Since A describes the modulation of the effective potential in the moiré cell, a

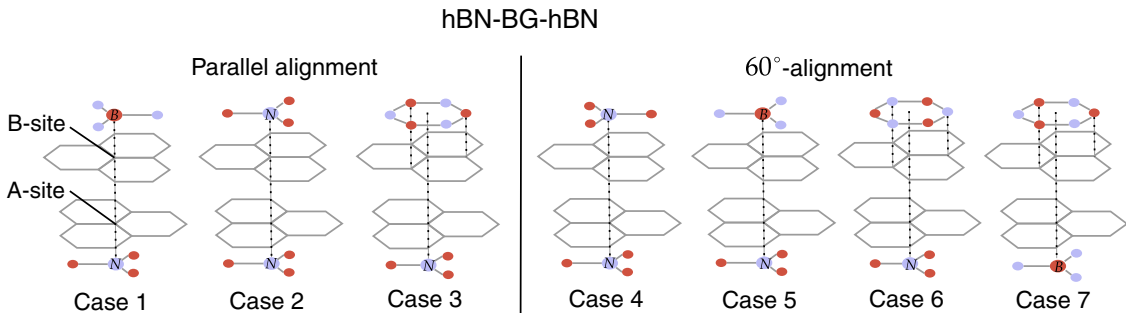


FIG. 3. Different stacking configurations of hBN-BG-hBN. In cases 1–3 the upper hBN layer is parallel to the lower hBN layer, and in cases 4–7 the upper hBN layer is rotated by 60°.

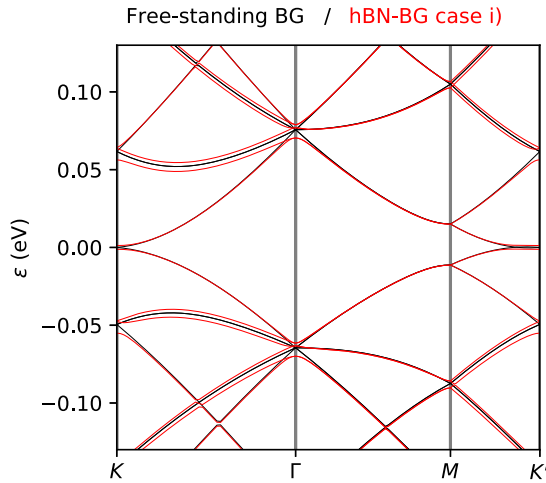


FIG. 4. Band structure of hBN-BG ($N_{\text{moiré}} = 56$, red lines) and free-standing BG (black lines) downfolded to the same mini Brillouin zone. At the K and K' points the hBN potential [Eq. (2)] creates secondary, gapped Dirac points at band energies $\epsilon \sim +0.06$ eV and $\epsilon \sim -0.05$ eV. In addition, a band gap opens at charge neutrality (see Fig. 5 for a zoom-in).

model with $A = 0$ has the same small unit cell size as BG. The C parameter causes an energy difference between A and B carbon sites in cases 1–3 and an energy difference between dimer and nondimer sites in cases 4–7 [42]. In Fig. 3 we see that in cases 1–3, the upper hBN layer is parallel to the lower layer (“parallel alignment”), whereas in cases 4–7 the upper hBN layer is rotated by 60° (“ 60° alignment”).

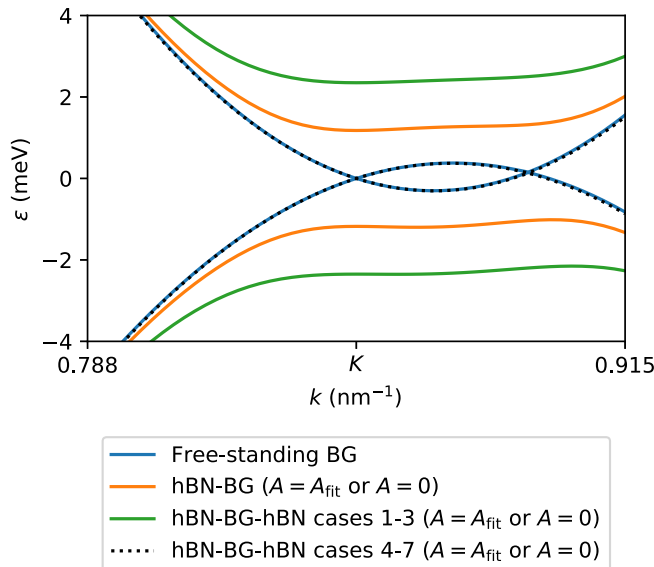


FIG. 5. Low-energy band structure near the K point of the mini Brillouin zone ($N_{\text{moiré}} = 20$). The band structure shows a band gap at charge neutrality for hBN-BG and for hBN-BG-hBN cases 1–3. This band gap originates from an energy difference at neighboring carbon sites. Although alignment of the hBN layer and development of the moiré structure is necessary for the band gap opening, the gap itself can be modeled in a small unit cell corresponding to $A = 0$ in the hBN potential Δ_r .

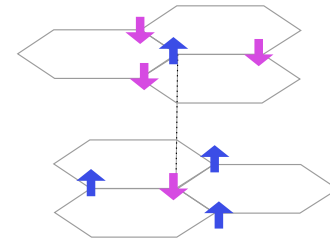


FIG. 6. In all of our calculations the dominant magnetic order is found to be antiferromagnetic with opposite signs of the magnetization at neighboring carbon sites. Besides the relative spatial ordering pattern, the orientation of the magnetization is not fixed as long as the spin-orbit interaction is not taken into account.

Next, we turn to the possibility of magnetic order in our structures, within the RPA approach described above. In all cases studied, the dominant magnetic order is interlayer and intralayer antiferromagnetic, as shown in Fig. 6. No noticeable variation of this antiferromagnetic order was found within the moiré cell as the relevant eigenvectors turned out to be very homogeneous in their magnitudes through the moiré cell. This is quite different from the twisted bilayer cases studied, e.g., in Refs. [40,43], where the eigenvectors vary strongly in the moiré cell.

Now, we calculate U_c for the different structures as a function of the temperature in Fig. 7. We find that the low-energy band structures of the noninteracting system fully determine the differences and the similarities between free-standing BG, hBN-BG, and hBN-BG-hBN. For free-standing BG and 60° -aligned hBN-BG-hBN, structures with band crossings at the Fermi energy, U_c continuously increases with the temperature. This is expected as thermal fluctuations at some point destroy

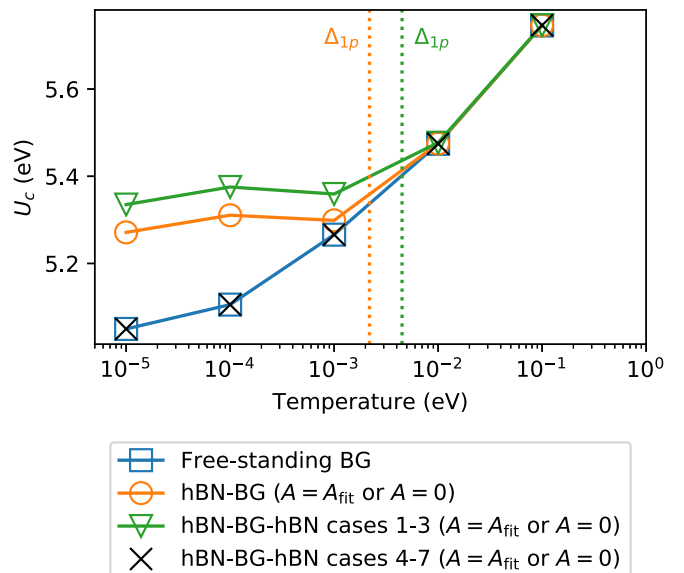


FIG. 7. Critical Hubbard interaction U_c for magnetic order as a function of the temperature ($N_{\text{moiré}} = 20$). The different stacking configurations differ in that for structures with a band gap (e.g., hBN-BG) at temperatures smaller than the band gap, U_c is larger as compared to structures without a band gap (e.g., free-standing BG).

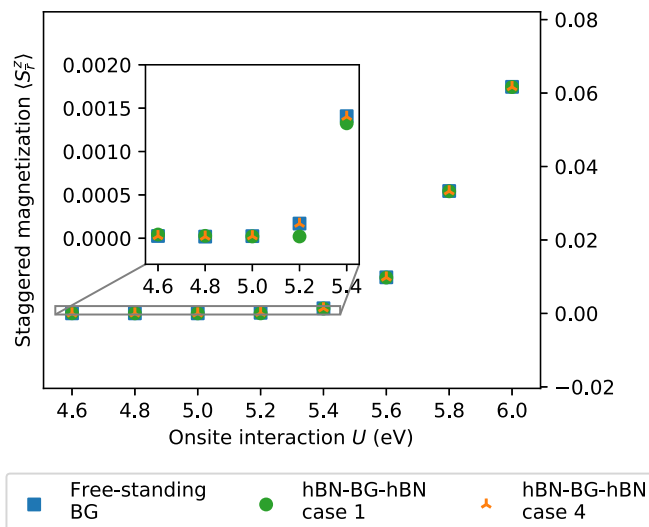


FIG. 8. Staggered magnetization in self-consistent mean-field theory as a function of the Hubbard interaction U at a temperature of $T = 10^{-4}$ eV ($N_{\text{moiré}} = 20$).

the magnetic order. For “substrate-gapped” structures such as hBN-BG or parallelly aligned hBN-BG-hBN, U_c differs from free-standing and 60° -aligned BG at temperatures below the size of the band gap. In this regime, U_c saturates at an approximately constant value. This behavior is consistent with the expectations that band structure gaps become visible at temperatures below these energy scales. Similar as in the analysis of the band structure, we see that the A parameter of the hBN potential does not play a role in our results. This means that, at least at charge neutrality, the moiré length scale does not influence the ordering tendency. In total, interaction effects are weakened by the substrate-induced band gap, although the difference in U_c is small.

Next, we evaluate the magnetic order of free-standing BG, hBN-BG-hBN case 1, and hBN-BG-hBN case 2 in mean-field theory at a temperature of $T = 10^{-4}$ eV. In Fig. 8 we show the magnetization (S_r^z) in its magnitude and plot its absolute value averaged over the moiré cell as a function of U . The critical interaction strength U_c needed to obtain a finite magnetization can be read off to be $5.0 \text{ eV} < U_c < 5.2 \text{ eV}$ for free-standing BG and hBN-BG-hBN case 2, and $5.2 \text{ eV} < U_c < 5.4 \text{ eV}$ for hBN-BG-hBN case 1. These values of U_c are in agreement with the RPA results described above. Next, we calculate the band structure of the converged mean-field Hamiltonian. In Fig. 9 we extract the band gap widths at charge neutrality, again for different values of the interaction strength. As commonly observed in Hubbard models [41], for parameters with nonzero magnetization an interaction-induced band gap is opened and we can see that the size of this band gap increases with the magnetization. In the nonmagnetic phase the structures are described by the noninteracting picture, which explains the band gap for low values of U in hBN-BG-hBN case 1. At $U = 5.2 \text{ eV}$ this substrate-induced band gap in case 1 is still larger than the interaction-induced band gap in free-standing and hBN-BG-hBN case 2. At $U = 5.4 \text{ eV}$ the interaction-induced band gaps of free-standing BG and hBN-BG-hBN case 2 exceed that of hBN-BG-hBN case 1.

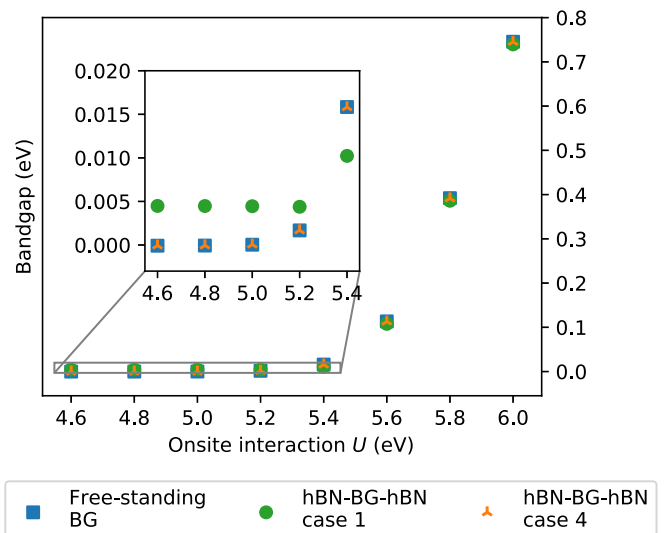


FIG. 9. Band gap sizes of the converged mean-field theory corresponding to Fig. 8 as a function of the Hubbard interaction U . For low U , the model can be described by the noninteracting system and only hBN-BG-hBN case 1 has a band gap. For large U the magnetic state results in larger “magnetic” band gaps in all structures.

IV. DISCUSSION

Both the RPA analysis and the mean-field calculation show an upward shift of U_c for substrate-gapped structures at low temperatures. Quantitatively, this shift is less than 6%, putting constraints on the possibility that instabilities of BG may be observed in free-standing bilayers but not in the heterostructures. Even in this small window, the systems that do not have an interaction-driven ordered ground state show a substrate-induced gap. Thus, if no gap is observed, one should deal with a case without substrate-induced gap where the effective on-site repulsion is too small to trigger a ground state change at the given temperature. Lowering the temperature could still open a gap, but this gap might be too small to be observed. Note that the trigonal warping terms split any quadratic band crossing points of simple bilayer band structures into Dirac points, such that at zero temperature there should be a nonzero threshold value in U for ordering.

We also discuss the justification and magnitude of the on-site repulsion used in the Hubbard modeling of this work. Clearly, a more realistic model should, beyond the on-site term, also include nonlocal interaction terms. This nonlocal interaction can approximately be incorporated in an effective on-site repulsion. In Ref. [38] such a simplification was analyzed in *ab initio* calculations employing the constrained random phase approximation and it is suggested to estimate the effective on-site interaction via $U \approx U_0 - U_1$, where U_0 is the “pure” on-site interaction and U_1 is the nearest-neighbor interaction. For free-standing BG a value of $U \approx 9.3 \text{ eV} - 4.7 \text{ eV} = 4.6 \text{ eV}$ would be obtained [33]. However, the hBN substrate may screen and thus reduce both the pure on-site interaction and the nearest-neighbor interaction as calculated in Ref. [33]. This screening from the substrate may approximately cancel out for the effective U and we get, again, $U \approx 8.3 \text{ eV} - 3.7 \text{ eV} = 4.6 \text{ eV}$. In all these approximations

we stay well below our threshold values for ordering, i.e., on the side where potential gaps would be induced by the hBN layers. This is however not consistent with the experimental reports of gaps in freely suspended Bernal-stacked systems [18–24]. Thus, we conclude that a quantitative description of these systems remains a challenge.

From the mean-field calculation we find that, while the band gaps of single-particle nature are less variable, the interaction-induced gap is a strongly varying function of U and largely independent of the putative noninteracting band structure once the interaction threshold is exceeded. This observation makes it difficult to compare our different materials, because the hBN-substrated materials may have a different effective U compared to free-standing BG due to the additional screening effects. Our mean-field results imply that the precise value of U will be the determining component for the size of the magnetic band gap. Further, we see that hBN-BG and parallelly aligned hBN-BG-hBN are gapped for all values of U . A case where the substrate destroys the ordering instability and the interaction-induced gap without producing another single-particle gap does not appear in our study.

V. SUMMARY

In summary, we identified several stacking configurations and differentiated between parallelly aligned and 60°-aligned

hBN-BG-hBN. The influence of hBN on the electronic structure of the BG was captured by an effective single-particle potential in analogy to earlier DFT work [34]. hBN-BG and parallelly aligned hBN-BG-hBN have a band gap of “single-particle” origin already in the noninteracting picture. For temperatures smaller than this band gap, the critical Hubbard interaction U_c required for a magnetic ordering is larger than for the 60°-aligned hBN-BG-hBN cases and free-standing BG. Thus interaction effects are weakened by the substrate-induced band structure changes. However, the shift in U_c is less than 6%. Mean-field theory allowed us to calculate the band gap sizes of the interacting systems. Our results demonstrate that the interaction-induced band gap is a strongly varying function of the on-site interaction U .

ACKNOWLEDGMENTS

The Deutsche Forschungsgemeinschaft (DFG, German Research Foundation) is acknowledged for support through RTG 1995, within the Priority Program SPP 2244 “2DMP” and under Germany’s Excellence Strategy-Cluster of Excellence Matter and Light for Quantum Computing (ML4Q) EXC2004/1 - 390534769. We acknowledge support from the Max Planck-New York City Center for Non-Equilibrium Quantum Phenomena. Calculations were performed with computing resources granted by RWTH Aachen University under project rwth0510.

-
- [1] M. Yankowitz, Q. Ma, P. Jarillo-Herrero, and B. J. LeRoy, *Nat. Rev. Phys.* **1**, 112 (2019).
- [2] L. Liu, Y. P. Feng, and Z. X. Shen, *Phys. Rev. B* **68**, 104102 (2003).
- [3] E. McCann and M. Koshino, *Rep. Prog. Phys.* **76**, 056503 (2013).
- [4] M. Yankowitz, J. Xue, D. Cormode, J. D. Sanchez-Yamagishi, K. Watanabe, T. Taniguchi, P. Jarillo-Herrero, P. Jacquod, and B. J. LeRoy, *Nat. Phys.* **8**, 382 (2012).
- [5] G. J. Slotman, M. M. van Wijk, P.-L. Zhao, A. Fasolino, M. I. Katsnelson, and S. Yuan, *Phys. Rev. Lett.* **115**, 186801 (2015).
- [6] J. Jung, A. M. DaSilva, A. H. MacDonald, and S. Adam, *Nat. Commun.* **6**, 6308 (2015).
- [7] J. C. W. Song, A. V. Shytov, and L. S. Levitov, *Phys. Rev. Lett.* **111**, 266801 (2013).
- [8] P. Moon and M. Koshino, *Phys. Rev. B* **90**, 155406 (2014).
- [9] C. Woods, L. Britnell, A. Eckmann, R. Ma, J. Lu, H. Guo, X. Lin, G. Yu, Y. Cao, R. Gorbachev *et al.*, *Nat. Phys.* **10**, 451 (2014).
- [10] L. Ponomarenko, R. Gorbachev, G. Yu, D. Elias, R. Jalil, A. Patel, A. Mishchenko, A. Mayorov, C. Woods, J. Wallbank *et al.*, *Nature (London)* **497**, 594 (2013).
- [11] B. Hunt, J. D. Sanchez-Yamagishi, A. F. Young, M. Yankowitz, B. J. LeRoy, K. Watanabe, T. Taniguchi, P. Moon, M. Koshino, P. Jarillo-Herrero, and R. C. Ashoori, *Science* **340**, 1427 (2013).
- [12] M. Bokdam, T. Amlaki, G. Brocks, and P. J. Kelly, *Phys. Rev. B* **89**, 201404(R) (2014).
- [13] Y.-H. Zhang, D. Mao, Y. Cao, P. Jarillo-Herrero, and T. Senthil, *Phys. Rev. B* **99**, 075127 (2019).
- [14] H. Kim, N. Leconte, B. L. Chittari, K. Watanabe, T. Taniguchi, A. H. MacDonald, J. Jung, and S. Jung, *Nano Lett.* **18**, 7732 (2018).
- [15] K. Endo, K. Komatsu, T. Iwasaki, E. Watanabe, D. Tsuya, K. Watanabe, T. Taniguchi, Y. Noguchi, Y. Wakayama, Y. Morita, and S. Moriyama, *Appl. Phys. Lett.* **114**, 243105 (2019).
- [16] M. Kuri, S. K. Srivastav, S. Ray, K. Watanabe, T. Taniguchi, T. Das, and A. Das, *Phys. Rev. B* **103**, 115419 (2021).
- [17] L. A. Gonzalez-Arraga, J. L. Lado, F. Guinea, and P. San-Jose, *Phys. Rev. Lett.* **119**, 107201 (2017).
- [18] J. Velasco Jr, L. Jing, W. Bao, Y. Lee, P. Kratz, V. Aji, M. Bockrath, C. N. Lau, C. Varma, R. Stillwell, D. Smirnov, F. Zhang, J. Jung, and A. H. MacDonald, *Nat. Nanotechnol.* **7**, 156 (2012).
- [19] W. Bao, L. Jing, J. Velasco, Jr., Y. Lee, G. Liu, D. Tran, B. Standley, M. Aykol, S. B. Cronin, D. Smirnov, M. Koshino, E. McCann, M. Bockrath, and C. N. Lau, *Nat. Phys.* **7**, 948 (2011).
- [20] F. Freitag, J. Trbovic, M. Weiss, and C. Schönenberger, *Phys. Rev. Lett.* **108**, 076602 (2012).
- [21] A. Veligura, H. J. van Elferen, N. Tombros, J. C. Maan, U. Zeitler, and B. J. van Wees, *Phys. Rev. B* **85**, 155412 (2012).
- [22] A. L. Grushina, D.-K. Ki, M. Koshino, A. A. L. Nicolet, C. Faugeras, E. McCann, M. Potemski, and A. F. Morpurgo, *Nat. Commun.* **6**, 6419 (2015).
- [23] Y. Nam, D.-K. Ki, D. Soler-Delgado, and A. F. Morpurgo, *Science* **362**, 324 (2018).
- [24] K. Myhro, S. Che, Y. Shi, Y. Lee, K. Thilakar, K. Bleich, D. Smirnov, and C. N. Lau, *2D Mater.* **5**, 045013 (2018).

- [25] F. Zhang, J. Jung, G. A. Fiete, Q. Niu, and A. H. MacDonald, *Phys. Rev. Lett.* **106**, 156801 (2011).
- [26] R. E. Throckmorton and O. Vafek, *Phys. Rev. B* **86**, 115447 (2012).
- [27] M. Kharitonov, *Phys. Rev. B* **86**, 195435 (2012).
- [28] J. Nilsson, A. H. Castro Neto, N. M. R. Peres, and F. Guinea, *Phys. Rev. B* **73**, 214418 (2006).
- [29] T. C. Lang, Z. Y. Meng, M. M. Scherer, S. Uebelacker, F. F. Assaad, A. Muramatsu, C. Honerkamp, and S. Wessel, *Phys. Rev. Lett.* **109**, 126402 (2012).
- [30] M. M. Scherer, S. Uebelacker, and C. Honerkamp, *Phys. Rev. B* **85**, 235408 (2012).
- [31] M. M. Scherer, S. Uebelacker, D. D. Scherer, and C. Honerkamp, *Phys. Rev. B* **86**, 155415 (2012).
- [32] C. Honerkamp, *Phys. Rev. Lett.* **100**, 146404 (2008).
- [33] M. Rösner, E. Şaşıoğlu, C. Friedrich, S. Blügel, and T. O. Wehling, *Phys. Rev. B* **92**, 085102 (2015).
- [34] B. Sachs, T. O. Wehling, M. I. Katsnelson, and A. I. Lichtenstein, *Phys. Rev. B* **84**, 195414 (2011).
- [35] G. Trambly de Laissardière, D. Mayou, and L. Magaud, *Nano Lett.* **10**, 804 (2010).
- [36] P. Moon and M. Koshino, *Phys. Rev. B* **85**, 195458 (2012).
- [37] A. Rozhkov, A. Sboychakov, A. Rakhmanov, and F. Nori, *Phys. Rep.* **648**, 1 (2016).
- [38] M. Schüler, M. Rösner, T. O. Wehling, A. I. Lichtenstein, and M. I. Katsnelson, *Phys. Rev. Lett.* **111**, 036601 (2013).
- [39] H.-K. Tang, E. Laksono, J. N. B. Rodrigues, P. Sengupta, F. F. Assaad, and S. Adam, *Phys. Rev. Lett.* **115**, 186602 (2015).
- [40] L. Klebl and C. Honerkamp, *Phys. Rev. B* **100**, 155145 (2019).
- [41] Y. Claveau, B. Arnaud, and S. D. Matteo, *Eur. J. Phys.* **35**, 035023 (2014).
- [42] M. Mucha-Kruczyński, E. McCann, and V. I. Fal'ko, *Semicond. Sci. Technol.* **25**, 033001 (2010).
- [43] L. Klebl, D. M. Kennes, and C. Honerkamp, *Phys. Rev. B* **102**, 085109 (2020).